Supplementary Information for

Acoustic Möbius insulators from projective symmetry

Tianzi Li,[1†] Juan Du,[1†] Qicheng Zhang, [1†] Yitong Li, Xiying Fan,[1] Fan Zhang,[2*] and Chunyin Qiu[1*]

[1]Key Laboratory of Artificial Micro- and Nano-Structures of Ministry of Education and School of Physics and Technology, Wuhan University, Wuhan 430072, China

[2]Department of Physics, University of Texas at Dallas, Richardson, Texas 75080, USA

[†] These authors contributed equally.

* To whom correspondence should be addressed: cyqiu@whu.edu.cn; zhang@utdallas.edu

Supplementary Note 1.

3D Möbius insulators (MIs) and 3D Möbius Dirac semimetals (MDSs)

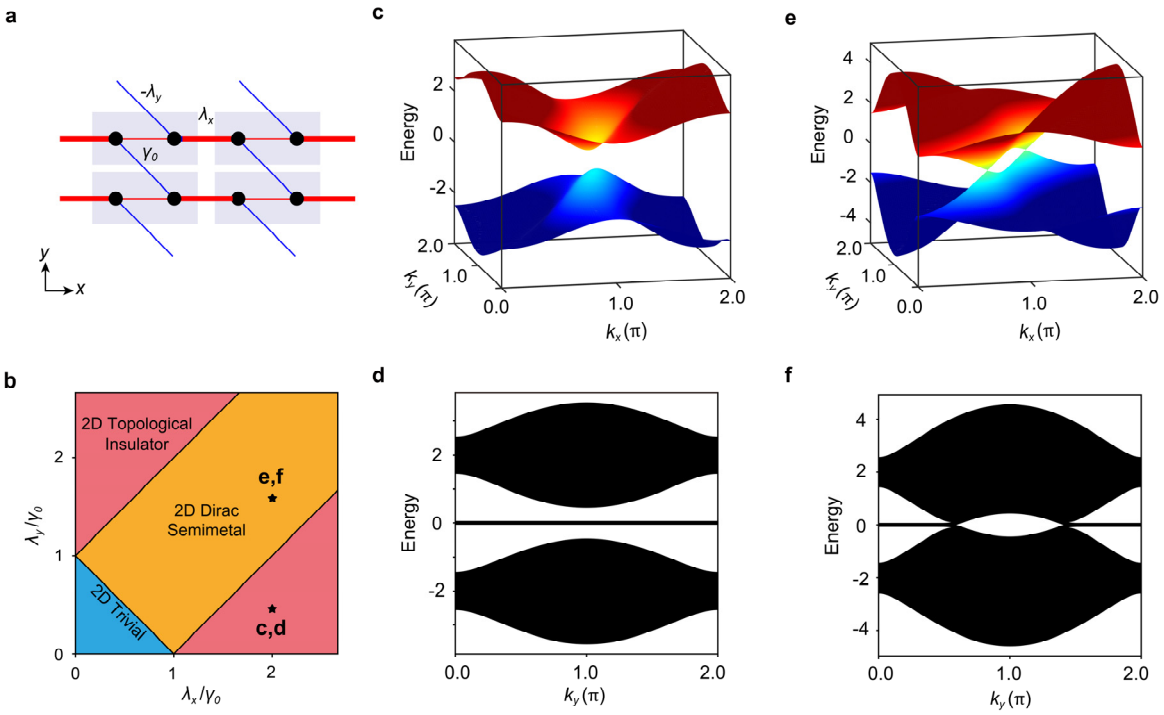

Figure S1 | Extended 2D SSH model. a, Tight-binding model. **b**, Phase diagram versus the coupling ratios λ_x/γ_0 and λ_y/γ_0, which exhibits the trivial insulator, topological insulator and Dirac semimetal phases. **c**, Bulk bands exemplified for the 2D topological insulator with $\gamma_0 = 1$, $\lambda_x = 2$, and $\lambda_y = 0.5$. **d**, The projected band structure along the k_y direction corresponding to **c**. **e**,**f**, Similar to **c** and **d**, but for the 2D Dirac semimetal with $\lambda_y = 1.5$ compared with the topological insulator case in **c** and **d**.

Here we propose a simple layer construction for 3D MIs and MDSs. As shown in Fig. S1a, the monolayer model is a 2D extension of the 1D Su-Schrieffer-Heeger (SSH) chain[1,2]. Its Hamiltonian reads

$$h_{2D} = (\gamma_0 + \lambda_x \cos k_x - \lambda_y \cos k_y)\sigma_1 + (\lambda_x \sin k_x - \lambda_y \sin k_y)\sigma_2, \qquad \text{(S1)}$$

where γ_0 is the intra-cell hopping, and λ_x and λ_y are the inter-cell hoppings along the x and y directions, respectively. Here we assume $\gamma_0, \lambda_x, \lambda_y > 0$. Note that the chiral symmetry is inherited from the SSH chains, since both the inter-cell hoppings λ_x and λ_y connect the sites of different sublattices. Figure S1b sketches the phase diagram versus the coupling ratios λ_x/γ_0 and λ_y/γ_0. Besides a trivial insulator phase, it includes two topological insulator phases and one (twofold degenerate) Dirac semimetal phase too[1]. The phase boundaries are defined by $\lambda_x = \gamma_0 + \lambda_y$, $\lambda_y = \gamma_0 + \lambda_x$, and $\gamma_0 = \lambda_x + \lambda_y$. Similar to the 1D SSH model, the insulating phases can be characterized by winding numbers, featuring 1D zero-energy edge states along the y (or x) direction in the case of $\lambda_x > \gamma_0 + \lambda_y$ (or $\lambda_y > \gamma_0 + \lambda_x$); the topology of the Dirac semimetal phase is characterized by k_y- and k_x- dependent winding numbers,

manifested as the 1D zero-energy edge states connecting the projected Dirac nodes. The above physics is exemplified in Fig. S1c-S1f with specific hopping parameters.

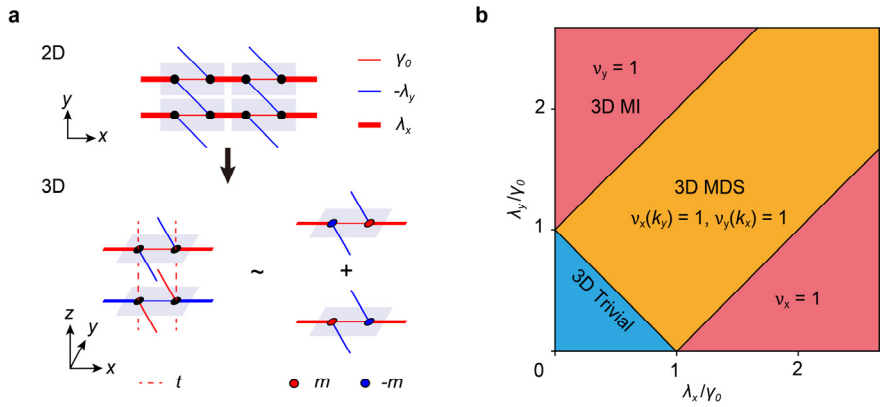

Figure S2 | Phase diagram for 3D MI and 3D MDS. a, A layered 3D model (left) and its effective decomposition (right), where all in-plane hopping signs are flipped every other layer. **b**, Phase diagram. The phase boundaries feature the generation or annihilation of fourfold degenerate Dirac points.

Figure S2a shows the model for constructing the 3D MI and 3D MDS, where the monolayer is descriped by Eq. (S1). The resulted 3D system has two $\mathbb{Z}_2$ topological invariants. Figure S2a (bottom right) also shows the equivalent model consisting of two decoupled sectors (distinguished with the eigenvalues of $\mathcal{L}_z$), each of which can be viewed as a 2D massive SSH model with $\pm m = \pm 2t\cos(k_z/2)$. Figure S2b shows the phase diagram of our 3D model, which inherits exactly from its monolayer one. That is, in addition to a 3D trivial insulator phase, it exhibits two 3D MI phases evolved from the topological insulator phases in 2D, and one 3D MDS phase evolved from the 2D Dirac semimetal phase. The parameters used to calculate the band structures for the 3D MI and the 3D MDS in the main text are $\gamma_0 = 1$, $\lambda_x = 2$, and $t = \lambda_y = 0.5$, and $\gamma_0 = 1$, $\lambda_x = 2$, $t = 0.5$, and $\lambda_y = 1.5$, respectively. The band topologies are characterized by nontrivial $\mathbb{Z}_2$ invariants ν_x and ν_y, which are simply extended from the 2D MI case.

Supplementary Note 2.

Construction of the topological invariants

First, we briefly introduce the theoretical derivation of the topological invariant for the 2D MI. Considering the commutation relation $[\mathcal{L}_z, H_{2D}] = 0$ and the fact that $\mathcal{L}_z$ can be diagonalized as $U_{2D}^{-1}\mathcal{L}_z U_{2D} = -e^{ik_z/2}\sigma_3\rho_0$, the 2D Hamiltonian H_{2D} (see main text) is block-diagonalizable, $U_{2D}^{-1}H_{2D}U_{2D} = h_{2D}^{+} \oplus h_{2D}^{-}$, where the unitary matrix $U_{2D} =$

$\begin{pmatrix} 0 & -e^{-\frac{ik_z}{2}} & 0 & e^{-\frac{ik_z}{2}} \\ e^{-\frac{ik_z}{2}} & 0 & -e^{-\frac{ik_z}{2}} & 0 \\ 0 & 1 & 0 & 1 \\ 1 & 0 & 1 & 0 \end{pmatrix}$ and $h_{2D}^{\pm} = \begin{pmatrix} \pm 2t\cos\frac{k_z}{2} & \gamma_x + \lambda_x e^{ik_x} \\ \gamma_x + \lambda_x e^{-ik_x} & \mp 2t\cos\frac{k_z}{2} \end{pmatrix}$. Strikingly, the diagonalized Hamiltonian consists of two copies of 1D massive SSH chains with opposite onsite energies along the x direction, described by h_{2D}^{+} and h_{2D}^{-}. A $\mathbb{Z}_2$ invariant ν can be defined[3] on any one of them (e.g. h_{2D}^{-} below),

$$\nu = \frac{1}{2\pi}\int_{\Omega} \mathcal{F} d^2k + \frac{1}{\pi}\gamma(k_{z0}) \bmod 2, \tag{S2}$$

where $\mathcal{F} = (\nabla_{\boldsymbol{k}} \times \mathcal{A})_y$ is Berry curvature of the valence band (described by the wavefunction ψ_V), with $\mathcal{A}(\boldsymbol{k}) = \langle \psi_V | i\nabla_{\boldsymbol{k}} | \psi_V \rangle$ being Berry connection, and $\gamma(k_{z0}) = \oint dk_x \mathcal{A}_x$ is Berry phase evaluated along the momentum loop with $k_z = k_{z0}$.[3] The integration region of the first term is specified as $\Omega = [k_{z0}, k_{z0} + 2\pi] \times S^1$, as shown in Fig. S3a, to emphasize the 4π periodicity of h_{2D}^{-} along the k_z direction. For simplicity, we set $k_{z0} = 0$ here (also for the following 3D cases). Note that, given the periodicity of h_{2D}^{-}, this $\mathbb{Z}_2$ invariant measures the obstruction of Stokes theorem in the half-Brillouin zone Ω.[3]

Now we extend the above derivation of topological invariant to the 3D MI and MDS, in which the translation operator is $\mathcal{L}_z = \begin{pmatrix} 0 & 1 \\ e^{ik_z} & 0 \end{pmatrix}\sigma_3$. Again, considering the commutation relation $[H_{3D}, \mathcal{L}_z] = 0$, the 3D Hamiltonian H_{3D} can be block-diagonalized in the two eigenspaces of $\mathcal{L}_z$ (Fig. S2a) via the unitary transformation $U_{3D}^{-1} H_{3D} U_{3D} = h_{3D}^{+} \oplus h_{3D}^{-}$, where $h_{3D}^{\pm}(k_x, k_y, k_z) = \begin{pmatrix} \pm 2t\cos\frac{k_z}{2} & \gamma_0 + \lambda_x e^{ik_x} - \lambda_y e^{ik_y} \\ \gamma_0 + \lambda_x e^{-ik_x} - \lambda_y e^{-ik_y} & \mp 2t\cos\frac{k_z}{2} \end{pmatrix}$ and the unitary matrix $U_{3D} = \begin{pmatrix} 0 & -e^{-\frac{ik_z}{2}} & 0 & e^{-\frac{ik_z}{2}} \\ e^{-\frac{ik_z}{2}} & 0 & -e^{-\frac{ik_z}{2}} & 0 \\ 0 & 1 & 0 & 1 \\ 1 & 0 & 1 & 0 \end{pmatrix}$. In this case, we can define the $\mathbb{Z}_2$ invariants ν_x and ν_y for the k_x-k_z and k_y-k_z planes, respectively. We consider ν_x first. Similar to the 2D MI case, as shown in Fig. S3b, we focus on h_{3D}^{-} and define ν_x for any projective translation symmetry-preserved momentum plane A with fixed $k_y = k_{y0}$,

$$\nu_x = \frac{1}{2\pi}\int_A d^2k \mathcal{F} + \frac{1}{\pi}\gamma(k_{y0}, 0) \bmod 2, \tag{S3}$$

where $\mathcal{F} = (\nabla_{\boldsymbol{k}} \times \mathcal{A})_y$ is Berry curvature of the valence band and $\gamma(k_{y0}, 0) = \oint dk_x \mathcal{A}_x$ is Berry phase evaluated along the specific momentum loop b (see the red arrow). Again, this $\mathbb{Z}_2$ invariant measures the obstruction of Stokes theorem in the half-Brillouin zone in the plane A. Note that the choice of k_{y0} is arbitrary (since H_{3D} always commutes with $\mathcal{L}_z$), as long as the system is gapped at that momentum plane. Specifically, the topological invariant $\nu_x = 1$

for $\lambda_x > \gamma_0 + \lambda_y$, which gives rise to Möbius surface states on the *y*-*z* surface. Similarly, ν_y can be defined on the projective translation symmetry-preserved momentum plane with fixed $k_x = k_{x0}$, and the topological invariant $\nu_y = 1$ for $\lambda_y > \gamma_0 + \lambda_x$, indicating Möbius surface states on the *x*-*z* surface. Figure S3c presents the numerical result for the 3D MI considered in the main text. It shows that $\nu_x = 1$ for any k_{y0} and $\nu_y = 0$ for any k_{x0}, indicating the existence of Möbius surface states only on the *y*-*z* surface. Unlike the $\mathbb{Z}_2$ invariants in a 3D MI, ν_x (ν_y) is k_{y0} (k_{x0}) dependent in the 3D MDS. This is exemplified in Fig. S3d. Specifically, the segment of k_{y0} with $\nu_x = 1$ coincides with the segment where Möbius surface states emerge at the *y*-*z* surface BZ (see main text). Meanwhile, there is a segment of k_{x0} with $\nu_y = 1$, which coincides with the segment where Möbius surface states emerge at the *x*-*z* surface BZ (not shown).

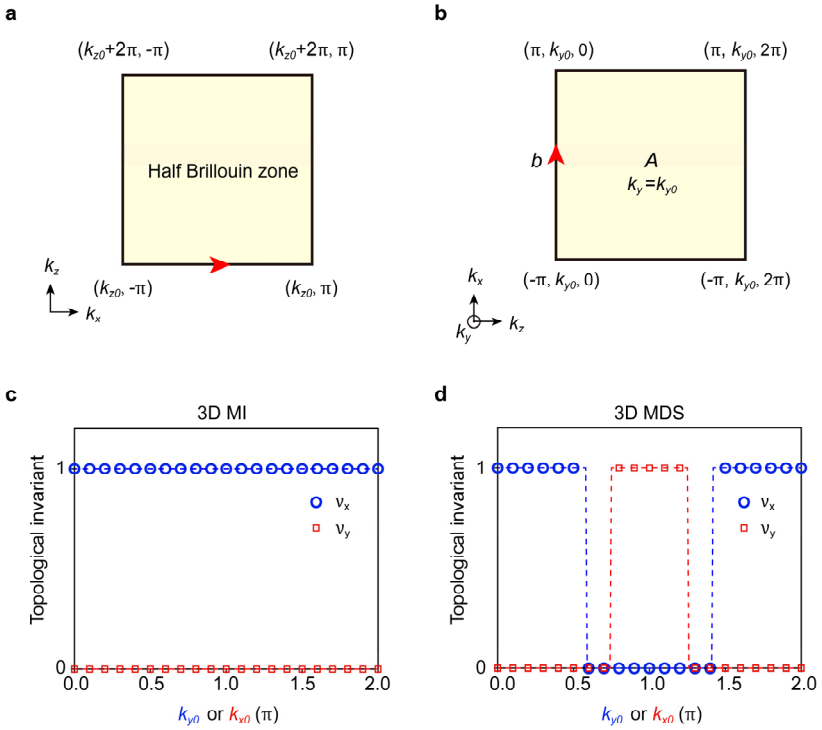

Figure S3 | Topological invariants for the 2D MI, 3D MI, and 3D MDS. a, The integration domain for evaluating the $\mathbb{Z}_2$ invariant ν for the 2D MI. The red arrow indicates the integration direction for the Berry phase $\gamma(k_{z0})$. **b**, The integration domain (with a fixed k_{y0}) for evaluating the $\mathbb{Z}_2$ invariant ν_x for the 3D MI. A similar treatment can be made for the calculation of ν_y. **c**, Numerical topological invariants ν_x and ν_y exemplified for the 3D MI considered in our main text. **d**, Similar to **c**, but for the MDS considered in the main text. The hoppings used for **c** and **d** are specified in the ***Supplementary Note 1***.

Finally, we introduce a higher-order version of the $\mathbb{Z}_2$ invariant for the 3D HOMI. As mentioned in the main text, the 3D HOMI is a periodic stack of the extensively studied

quadrupole model[4,5]. For the 2D quadrupole model, the topological invariant (quadrupole moment) can be viewed as the quantized polarization defined for Wannier bands. We follow this picture and extend the $\mathbb{Z}_2$ invariants above to a Wannier version $\tilde{\boldsymbol{\nu}}$. Again, we split the Hamiltonian of the 3D HOMI (Fig. 2d in the main text) into $h_{3D}^{+} \oplus h_{3D}^{-}$, associated with

$$h_{3D}^{\pm}(k_x,k_y,k_z)=\begin{pmatrix} \pm 2t\cos\frac{k_z}{2} & -\gamma_x-\lambda_x e^{ik_x} & \gamma_y+\lambda_y e^{ik_y} & 0 \\ -\gamma_x-\lambda_x e^{-ik_x} & \mp 2t\cos\frac{k_z}{2} & 0 & -\gamma_y-\lambda_y e^{ik_y} \\ \gamma_y+\lambda_y e^{ik_y} & 0 & \mp 2t\cos\frac{k_z}{2} & -\gamma_x-\lambda_x e^{ik_x} \\ 0 & -\gamma_y-\lambda_y e^{-ik_y} & -\gamma_x-\lambda_x e^{-ik_x} & \pm 2t\cos\frac{k_z}{2} \end{pmatrix}.$$

Here we focus on the sector h_{3D}^{-}, which can be viewed as a modified quadrupole model with staggered onsite energies. Similar to the case of 3D MI, we can define two $\mathbb{Z}_2$ invariants $\tilde{\nu}_x$ and $\tilde{\nu}_y$ on the k_x-k_z and k_y-k_z momentum planes, respectively. We consider $\tilde{\nu}_x$ in the following, and $\tilde{\nu}_y$ can be obtained similarly. According to Ref. 4, one can define the Wannier band subspaces $|w_{x,k}^{\pm}\rangle=\sum_{n=1,2}|u_k^n\rangle[v_{x,k}^{\pm}]^n$ by diagonalizing the Wilson loop operator, where $[v_{x,k}^{\pm}]^n$ is the n-th component of the eigenstates of the Wilson-loop operator, and $|u_k^n\rangle$ is the corresponding occupied state of h_{3D}^{-}. Note that here the Wannier band is k_x and k_z dependent in 2D momentum space. Therefore, similar to the definition of the $\mathbb{Z}_2$ invariants for the 3D MI, $\tilde{\nu}_x$ can be defined as

$$\tilde{\nu}_x=\frac{1}{2\pi}\int_A d^2k\tilde{\mathcal{F}}+\frac{1}{\pi}\tilde{\gamma}(0) \bmod 2, \tag{S4}$$

Where $\tilde{\mathcal{F}}=(\nabla_{\boldsymbol{k}}\times\tilde{\mathcal{A}})_y$ is the Berry curvature defined for the valence Wannier band $w_{x,k}^{-}$, with $\tilde{\mathcal{A}}(\boldsymbol{k})=\langle w_{x,k}^{-}|i\nabla_{\boldsymbol{k}}|w_{x,k}^{-}\rangle$ being the associated Berry connection, and $\tilde{\gamma}(0)=\oint dk_x\tilde{\mathcal{A}}_x$ is Berry phase defined in the Wannier subspace with fixed $k_z=0$. The integration region A is a momentum plane similar to the 3D MI case (see Fig. S3b), which emphasizes the 4π periodicity of the Wannier band along the k_z-direction.

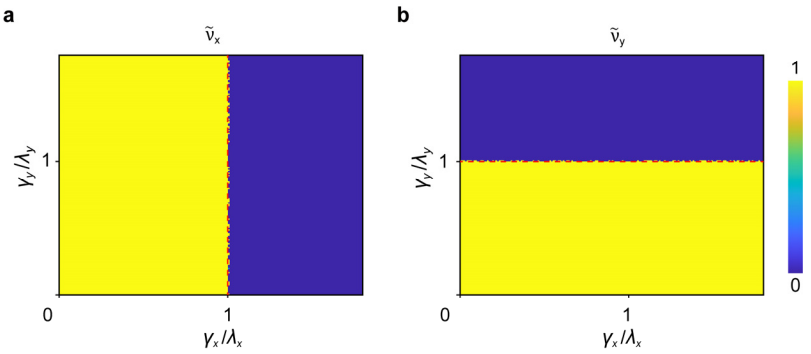

Figure S4 | Topological invariants calculated for the 3D HOMI. a, $\tilde{\nu}_x$ (color) versus the coupling ratios γ_x/λ_x and γ_y/λ_y. The red dashed line denotes the theoretically predicted phase boundary, which features zero Wannier gap. **b**, The same as **a**, but for $\tilde{\nu}_y$.

Figure S4 shows our numerical results for the two $\mathbb{Z}_2$ invariants $\tilde{\nu}_x$ and $\tilde{\nu}_y$ versus the coupling ratios γ_x/λ_x and γ_y/λ_y, which are quantized and change values when the corresponding Wannier bandgap closes and reopens (red dashed lines). The combination of Fig. S4a and Fig. S4b yields the phase diagram. Note that this model can be viewed as a critical point of the octupole topological insulator when there is no dimerization along the *z* direction, previously characterized by the octupole moments[4-7]. The phase boundary revealed by the $\mathbb{Z}_2$ invariants $\tilde{\nu}_x$ and $\tilde{\nu}_y$ coincide with the previous results obtained by the octupole moments.

Supplementary Note 3.
Acoustic designs of the 2D MI and 3D HOMI systems

Physically, the tight-binding models can be implemented with cavity-tube structures in acoustic systems[6-8], where the cavity resonators emulate atomic orbitals and the narrow tubes introduce hoppings between them. The onsite energy depends mostly on the geometry of the cavity, while the hopping strength depends mostly on the size of the connecting tubes. Interestingly, the key ingredient of the tight-binding model (i.e., π-flux) to achieve the $\mathbb{Z}_2$-projective translation symmetry can be easily realized in our acoustic crystals, in which the sign of hoppings is controlled by the connectivity of the coupling tubes[6]. Airborne sound is considered inside the whole structure, whose walls are regarded as acoustically rigid due to the large impedance mismatch to air. Throughout this work, air density $\rho = 1.29\ \mathrm{kg\,m^{-3}}$ and sound speed $c = 344.8\ \mathrm{m\,s^{-1}}$ are used for full-wave simulations, performed with the commercial software COMSOL Multiphysics (Pressure Acoustics Module).

Figures S5a and S5d demonstrate the detailed unit-cell geometries of our acoustic MI in 2D and HOMI in 3D, respectively. Specifically, each cuboid cavity resonator has a size of $30\ \mathrm{mm} \times 15\ \mathrm{mm} \times 8\ \mathrm{mm}$, which ensures a dipole resonance of frequency ~5746 Hz far away from the other undesired cavity modes. For our 2D MI structure, the lattice constants are $a = c = 75\ \mathrm{mm}$, and the square tubes of widths $w_1 = 3\ \mathrm{mm}$ and $w_2 = 7\ \mathrm{mm}$ correspond to the couplings $t = \gamma_x$ and λ_x in the tight-binding model. For our 3D HOMI system, the lattice constants are $a = c = 72.6\ \mathrm{mm}$ and $c = 43.6\ \mathrm{mm}$, and the widths of the square tubes are $w_1 = 1.8\ \mathrm{mm}$ and $w_2 = 5.0\ \mathrm{mm}$ in the *x*-*y* plane and $w_3 = 2.2\ \mathrm{mm}$ along the *z* direction, which correspond to the couplings $\gamma_x = \gamma_y$ and $\lambda_x = \lambda_y$ and t, respectively. In both cases, the sign of the hoppings, controlled by the spatial positions of the coupling tubes with respect to the cavities, is consistent with those depicted in Figs. 2a and 2d (see main text).

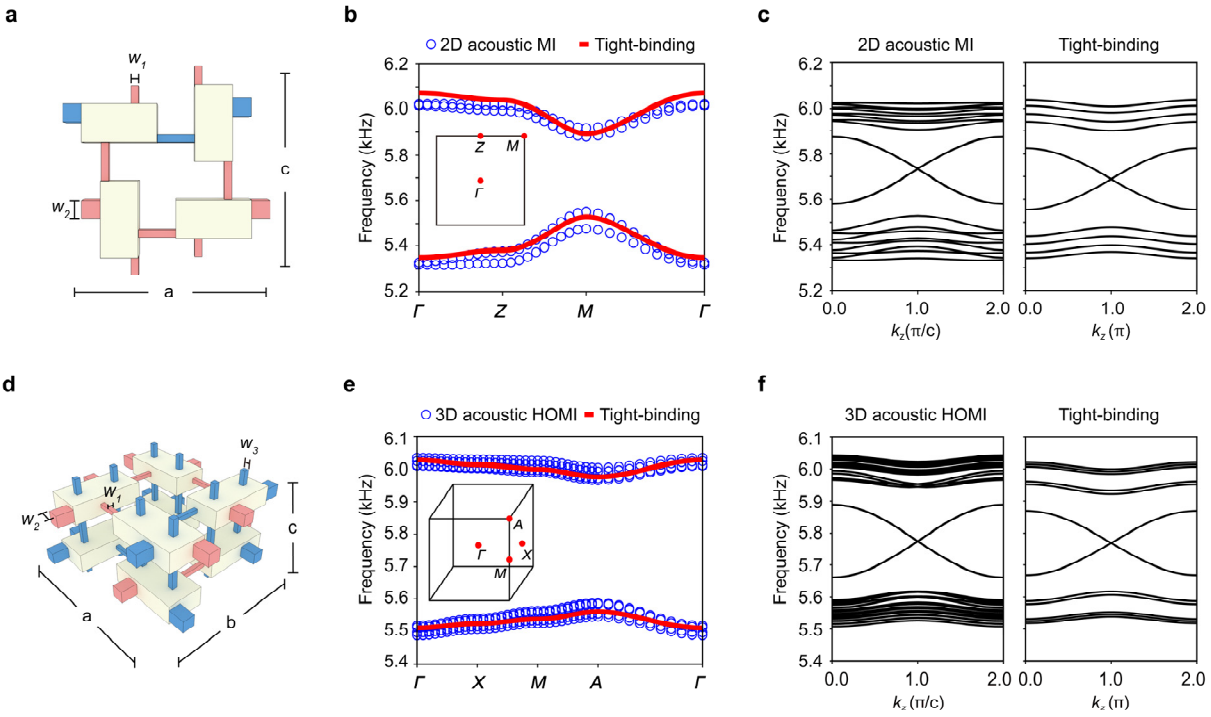

Figure S5 | Acoustic constructions of the 2D MI and 3D HOMI. **a**, Unit-cell geometry of the 2D acoustic MI, where the connecting tubes corresponding to positive and negative couplings are marked in red and blue, respectively. **b**, Bulk band structure of the designed 2D acoustic MI (blue circles), compared with the result of tight-binding modelling (red lines). **c**, Projected spectra of the 2D acoustic MI (left) and its comparative result of tight-binding modelling (right). **d-f**, Similar to **a-c**, but for the 3D HOMI.

We fit the effective parameters (onsite energy and hoppings) based on the bulk dispersion simulated with COMSOL Multiphysics, in which high-symmetry momenta are particularly taken into accounted. Figures S5b and S5e show the bulk band structures of our 2D MI and 3D HOMI, respectively. Notice that the numerical bulk bands are not strictly twofold degenerate as predicted by theory, due to the presence of unavoidable long-range and inter-mode couplings that weakly break the symmetries in the real structures. (This effect may be reduced by introducing more narrower coupling tubes and using the resonant cavity modes far away from the others.) Therefore, to fit the bulk dispersion as a whole, we consider the average frequency of the split bands. For the case of 2D MI, we fit the onsite energy $f_0 = \frac{1}{2}(f_\Gamma + f_M)$, where f_Γ and f_M are average frequencies of the conduction and valence bands at the Γ and M points, respectively. We also fit the hoppings based on the relations $\lambda_x - \gamma_x = \frac{1}{2}\Delta_M$ and $\lambda_x + \gamma_x = \frac{1}{2}\Delta_Z$ achieved from the eigen problem, where Δ_M and Δ_Z are respectively the band gaps at the M and Z points. For the 3D HOMI, we fit the onsite energy $f_0 = \frac{1}{2}(f_\Gamma + f_A)$, and the hoppings based on the relations $\sqrt{2(\lambda_y + \gamma_y)^2 + 4t^2} = \frac{1}{2}\Delta_\Gamma$, $\sqrt{2(\lambda_y - \gamma_y)^2 + 4t^2} = \frac{1}{2}\Delta_M$, and $\sqrt{2}(\lambda_y - \gamma_y) = \frac{1}{2}\Delta_A$, where all the notions follow the convention above. Note that for

simplicity we have used the same coupling tubes to simulate the hoppings γ_x and t in the 2D MI case, and the same coupling tubes to simulate the hoppings γ_x (λ_x) and γ_y (λ_y) in the 3D HOMI case. Through extracting the eigenfrequencies at high-symmetry momenta from the numerical band structures, the fitting process leads to $f_0 \approx 5689$ Hz, $t = \gamma_x \approx 68$ Hz and $\lambda_x \approx 261$ Hz for our 2D MI, and $f_0 \approx 5769$ Hz, $t \approx 50$ Hz, $\gamma_x = \gamma_y \approx 11$ Hz, and $\lambda_x = \lambda_y \approx 157$ Hz for our 3D HOMI. Note that the onsite energies for the coupled 2D and 3D structures slightly deviate (less than 1%) from that estimated with a single cavity resonator.

As shown in Fig. S5b and Fig. S5e, the full-wave simulated bulk bands (blue circles) are fitted well by the results (red lines) calculated from the tight-binding models with the effective hoppings and onsite energies. Note that the numerical bulk bands are not strictly symmetrical about the central frequency f_0, and also not strictly twofold (or fourfold) degenerate, owing to the presence of longer-range couplings and couplings to other cavity modes. These unwanted effects can be reduced through an optimization process[6]. The effectiveness of the fitting parameters is further demonstrated in the edge and hinge spectra in Fig. S5e and Fig. S5f.

Supplementary Note 4.
Acoustic response to local excitations for the 2D MI

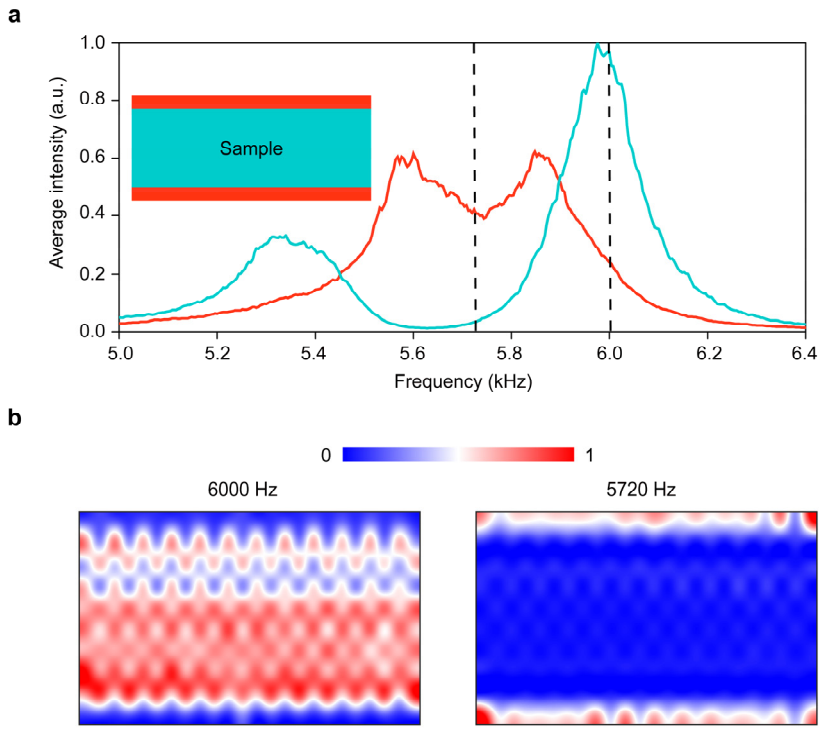

Figure S6 | Experimental acoustic response to local excitations in the 2D MI. a, Normalized bulk (cyan) and edge (red) spectra of the 2D MI, measured respectively at the sites colored in the inset. **b**, Intensity profiles extracted at two representative frequencies, exhibiting unambiguously as bulk (6000 Hz) and edge (5720 Hz) states.

We have also measured the acoustic response to local excitations[6,7] in the 2D MI. Instead of using the sample considered in the main text, here we consider a narrower sample (with all others being the same). Figure S6a shows the average intensity spectra extracted for the bulk and edge regions (see inset). The results coincide with the simulated band structure in Fig. S5c. Note that the edge spectrum (red line) exhibits a moderate dip around 5720 Hz due to the lower density of states in the middle of the edge bands, while the two peaks correspond to the frequency edges of the edge bands. The presence of the Möbius edge states can be further demonstrated in Fig. S6b, the intensity profile plotted at 5720 Hz (right panel), which is in sharp contrast to the bulk states plotted at 6000 Hz (left panel).

Supplementary Note 5.
Experimental scheme for detecting the eigenvalues of the projective translation symmetry

Here we describe the experimental scheme for detecting the eigenvalues of the projective translation symmetry. We focus on the 2D MI case and a similar treatment can be done for the 3D HOMI system.

In general, an edge state can be written in the form of $|\psi\rangle = (\phi_A, \phi_B, \phi_C, \phi_D)^T$, where ϕ_i represents the component of the sublattice i ($i = A\sim D$, as labeled in the inset of Fig. S7a). For brevity, the exponential decay of the eigenstate away from the sample edge is not explicitly expressed. When the projective translation operator $\mathcal{L}_z = \sigma_3 \begin{pmatrix} 0 & 1 \\ e^{ik_z} & 0 \end{pmatrix}$ acts on $|\psi\rangle$, we have

$$\mathcal{L}_x|\psi\rangle = \left(\phi_B, \phi_A e^{ik_z}, -\phi_D, -\phi_C e^{ik_z}\right)^T = \ell_s(\phi_A, \phi_B, \phi_C, \phi_D)^T, \tag{S5}$$

where $\ell_s = se^{ik_z/2}$ ($s = \pm$) are the eigenvalues of $\mathcal{L}_z$. Therefore, the eigenvalues ℓ_s can be written in terms of ϕ_A and ϕ_B (i.e., $\ell_s = \phi_B/\phi_A = \phi_A e^{ik_z}/\phi_B$) or in terms of ϕ_C and ϕ_D (i.e., $\ell_s = -\phi_D/\phi_C = -\phi_C e^{ik_z}/\phi_D$). In real measurements, we prefer $\ell_s = \phi_B/\phi_A$ or $\ell_s = -\phi_D/\phi_C$ for compactness. More specifically, we apply $\ell_s = \phi_B/\phi_A$ for the bottom edge and $\ell_s = -\phi_D/\phi_C$ for the top edge, considering the facts that the edge state concentrates on the sublattices A and B at the bottom edge and on the sublattices C and D at the top edge (as exemplified in Fig. S7b), respectively.

Notice that the eigenvalue winding can be fully reflected by its phase evolution in the frequency-momentum spectrum, since the magnitude of ℓ_s is always unitary. More explicitly, we can extract the phase of eigenvalue, $\arg(\ell_s)$, according to the formulae

$$\arg(\ell_s) = \arg(\phi_D) - \arg(\phi_C) + \pi, \tag{S6a}$$

$$\arg(\ell_s) = \arg(\phi_B) - \arg(\phi_A), \tag{S6b}$$

for the top and bottom edges, respectively. Therefore, the phase information of ℓ_s can be simply obtained from the phase difference between two different sublattices in a *single* unit cell, which greatly facilitates our experimental identification for the phase signature of the Möbius edge states. Below, assisted with a detailed numerical example, we demonstrate how the eigenvalue's phase evolution is measured in our experiments.

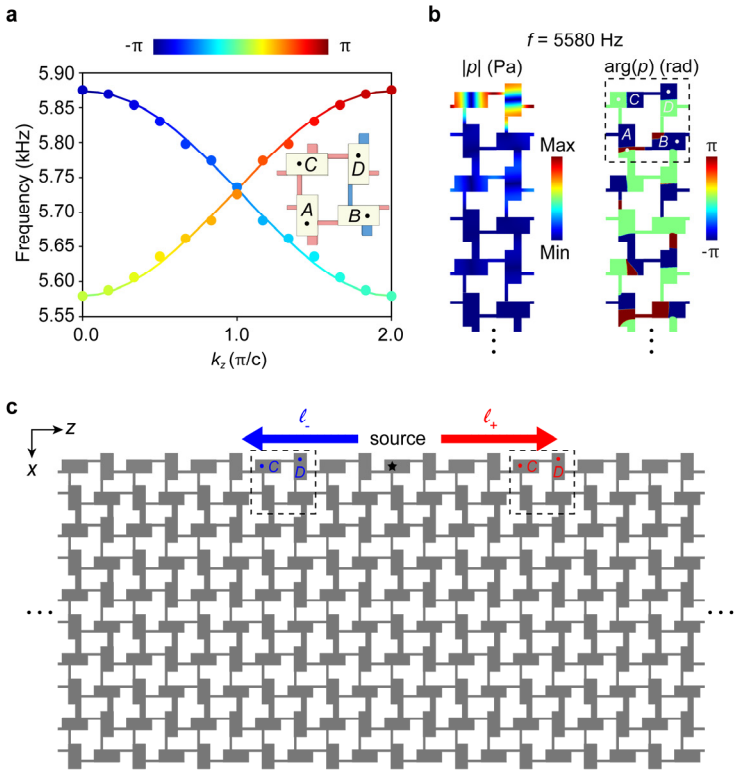

Figure S7 | Detecting the eigenvalues of the projective translation symmetry. a, Phase winding (color) of the eigenvalues $\ell_{\pm}$ encoded to the edge state dispersions (symbols). The color lines are simulated with a ribbon structure finite in the x direction but periodical in the z direction, and the color circles are simulated with a sample finite in both directions. Inset: Unit-cell geometry, labeled by four sublattices $A\sim D$. **b**, Amplitude (left) and phase (right) patterns for an edge state simulated with the ribbon structure. It shows that the pressure field concentrates on the sublattices C and D for the top edge state of the sample. Note that here we intentionally consider 5580 Hz (associated with $k_z = 0$ or equivalently $k_z = 2\pi/c$) to show the out-of-phase pattern on the sublattices C and D, which leads to $\arg(\ell_s) = 0$ or equivalently 2π [see Eq. (S6a)]. **c**, Numerical setup for extracting the band structure of the edge states and the associated phase information of ℓ_s. The former is obtained by Fourier transforming the pressure fields of all equivalent C and D sublattices along the top edge, while the latter is simply obtained from the C and D sublattices marked in the sample.

Take the top edge as an example. Figure S7c shows our numerical setup, which resembles the experimental one in Fig. 3a (see main text). An acoustic point-source is positioned in the middle of the top edge, which excites the edge states propagating in the $\pm z$ directions simultaneously. Specifically, the rightward- and leftward-propagating edge states correspond to the ℓ_+ and ℓ_- sectors, respectively. Therefore, one can detect the ℓ_+-locked and ℓ_--valued edge states in the right and left sample regions, respectively. (Note that reflections of the edge states from the lateral ends can be ignored thanks to the presence of the propagation

dissipation in real experiments. This is captured in our full-wave simulations by adding a tiny imaginary part to the sound speed.) To identify the Möbius twist in ℓ_s in the frequency-momentum space, we first acquire the numerical band structure of the 1D edge states, which can be obtained from spatial Fourier transform like that implemented for our experiments (that is, for each momentum k_z we extract the peaked frequency as 'eigenfrequency'). Then, we calculate $\arg(\ell_s)$ at each (k_z-dependent) 'eigenfrequency' according to Eq. (S6a) by using the phases extracted from the sublattices C and D in any given unit away from the source (see Fig. S7c). Figure S7a shows the numerical band structure (color dots) encoded with the phase information of the eigenvalues ℓ_s. It reproduces well the eigenproblem result (color lines) calculated for a perfect structure periodic in the z direction.

Reference

1. Palyi, A. Lecture notes: Topological semimetals (2017). https://physics.bme.hu/sites/physics.bme.hu/files/users/BMETE11MF34_kov/weyl_semimetals.pdf.
2. Khalaf, E., Benalcazar, W. A., Hughes, T. L. & Queiroz, R. Boundary-obstructed topological phases. *Phys. Rev. Research* **3**, 013239 (2021).
3. Zhao, Y., Huang, Y.-X. & Yang, S. A. Z_2-projective translational symmetry protected topological phases. *Phys. Rev. B* **102**, 161117 (2020).
4. Benalcazar, W. A., Bernevig, B. A. & Hughes, T. L. Quantized electric multipole insulators. *Science* **357**, 61-66 (2017).
5. Benalcazar, W. A., Bernevig, B. A. & Hughes, T. L. Electric multipole moments, topological multipole moment pumping, and chiral hinge states in crystalline insulators. *Phys. Rev. B* **96**, 245115 (2017).
6. Xue, H. et al. Observation of an acoustic octupole topological insulator. *Nat. Commun.* **11**, 2442 (2020).
7. Ni, X., Li, M., Weiner, M., Alù, A. & Khanikaev, A. B. Demonstration of a quantized acoustic octupole topological insulator. *Nat. Commun.* **11**, 2108 (2020).
8. Qi, Y. et al. Acoustic realization of quadrupole topological insulators. *Phys. Rev. Lett.* **124**, 206601 (2020).